
MIXTURE-OF-EXPERTS VARIATIONAL AUTOENCODER FOR CLUSTERING AND GENERATING FROM SIMILARITY-BASED REPRESENTATIONS ON SINGLE CELL DATA

A PREPRINT

Andreas Kopf^{1,5}, Vincent Fortuin^{2,4}, Vignesh Ram Somnath¹ & Manfred Claassen^{3#}

¹Institute of Molecular Systems Biology, Department of Biology, ETH Zürich, Switzerland.

²Biomedical Informatics Group, Department of Computer Science, ETH Zürich, Switzerland.

³Division of Clinical Bioinformatics, Department of Internal Medicine I, University of Tübingen, Tübingen, Germany.

⁴Swiss Institute of Bioinformatics (SIB), Switzerland.

⁵Life Science Graduate School Zurich, PhD Program Systems Biology, Switzerland.

manfred.claassen@med.uni-tuebingen.de

December 21, 2020

ABSTRACT

Clustering high-dimensional data, such as images or biological measurements, is a long-standing problem and has been studied extensively. Recently, Deep Clustering has gained popularity due to its flexibility in fitting the specific peculiarities of complex data. Here we introduce the Mixture-of-Experts Similarity Variational Autoencoder (MoE-Sim-VAE), a novel generative clustering model. The model can learn multi-modal distributions of high-dimensional data and use these to generate realistic data with high efficacy and efficiency. MoE-Sim-VAE is based on a Variational Autoencoder (VAE), where the decoder consists of a Mixture-of-Experts (MoE) architecture. This specific architecture allows for various modes of the data to be automatically learned by means of the experts. Additionally, we encourage the lower dimensional latent representation of our model to follow a Gaussian mixture distribution and to accurately represent the similarities between the data points. We assess the performance of our model on the MNIST benchmark data set and challenging real-world tasks of clustering mouse organs from single-cell RNA-sequencing measurements and defining cell subpopulations from mass cytometry (CyTOF) measurements on hundreds of different datasets. MoE-Sim-VAE exhibits superior clustering performance on all these tasks in comparison to the baselines as well as competitor methods.

Keywords Mixture-of-Experts · Variational Autoencoder · Clustering · Data generation

Author summary

Clustering single cell measurements into relevant biological phenotypes, such as cell types or tissue types, is an important task in computational biology. We developed a computational approach which allows incorporating prior knowledge about the single cell similarity into the training process, and ultimately achieve significant better clustering performance compared to baseline methods. This single cell similarity can be defined to benefit specific needs of the modeling goal, for example to either cluster cell type or tissue type, respectively.

In addition, we are able to generate new realistic single cell data from a respective mode of the phenotype due to the architecture of the model, which consists of smaller sub-models learning the different modes of the data. Compared to competitor methods, we show significantly better results on clustering and generation of handwritten digits of the MNIST data set, on clustering seven different mouse organs from single-cell RNA sequencing measurements, and on clustering cell types in over 272 different datasets of Peripheral Blood Mononuclear Cell measured via CyTOF.

Introduction

Clustering has been studied extensively [1, 20] in machine learning and has found wide application in identifying grouping structure in high dimensional biological data such as various omics data modalities. Recently, many Deep Clustering approaches were proposed, which modified (Variational) Autoencoder ((V)AE) architectures [20, 21] or by varying regularization of the latent representation [7, 2, 19, 33].

The reconstruction error usually drives the definition of the latent representation learned from an AE or VAE. The representation for AE models is unconstrained and typically places data objects close to each other according to an implicit similarity measure that also yields favorable reconstruction error. In contrast, VAE models regularize the latent representation such that the represented inputs follow a certain variational distribution. This construction enables sampling from the latent representation and data generation via the decoder of a VAE. Typically, the variational distribution is assumed standard Gaussian, but for example Jiang *et al.* [2] introduced a mixture-of-Gaussians variational distribution for clustering purposes.

A key component of clustering approaches is the choice of similarity metric for the considered data objects which we try to group [23]. Such similarity metrics are either defined *a priori* or learned from the data to specifically solve classification tasks via a Siamese network architecture [22]. Dimensionality reduction approaches, such as UMAP [3] or t-SNE [24], allow to specify a similarity metric for projection and thereby define the data separation in the inferred latent representation.

In this work, we introduce the Mixture-of-Experts Similarity Variational Autoencoder (MoE-Sim-VAE), a new deep architecture that performs similarity-based representation learning, clustering of the data and generation of data from each specific data mode. Due to a combined loss function, it can be jointly optimized. We empirically assess the scope of the model and present superior clustering performance on the canonical benchmark MNIST. Moreover, in an ablation study, we show the efficiency and precision of MoE-Sim-VAE for data generation purposes in comparison to the most related state-of-the-art method [2]. We achieve superior results on the identification of tissue- or cell type groupings via MoE-Sim-VAE on a murine single-cell RNA-sequencing atlas and mass cytometry measurements of Peripheral Blood Mononuclear Cells.

Materials and methods

MoE-Sim-VAE

Here we introduce the Mixture-of-Experts Similarity Variational Autoencoder (MoE-Sim-VAE, Figure 1). The model is based on the Variational Autoencoder [16]. While the encoder network is shared across all data points, the decoder of the MoE-Sim-VAE consists of a number of K different subnetworks, forming a Mixture-of-Experts architecture [6]. Each subnetwork constitutes a generator for a specific data mode and is learned from the data.

The variational distribution over the latent representation is defined to be a mixture of multivariate Gaussians, first introduced by Jiang *et al.* [2]. In our model, we aim to learn the mixture components in the latent representation to be standard Gaussians

$$\mathbf{z} \sim \sum_{k=0}^K \omega_k \mathcal{N}(\boldsymbol{\mu}_k, \mathbf{I}) \quad (1)$$

where ω_k are mixture coefficients, $\boldsymbol{\mu}_k$ are the means for each mixture component, \mathbf{I} is the identity matrix and K is the number of mixture components. The dimension of the latent representation z needs to be defined to suit the demands of Gaussian mixtures which have limitations in higher dimensions [35]. Similar to optimizing an Evidence Lower Bound (ELBO), we penalize the latent representation via the reconstruction loss of the data $\mathcal{L}_{reconst}$ and by using the Kullback-Leibler (KL) divergence for multivariate Gaussians [2] on the latent representation

$$\begin{aligned} \mathcal{L}_{KL} = D_{KL}(\mathcal{N}_0, \mathcal{N}_1) = & \frac{1}{2} \{tr(\boldsymbol{\Sigma}_1^{-1} \boldsymbol{\Sigma}_0) + \\ & (\boldsymbol{\mu}_1 - \boldsymbol{\mu}_0)^T \boldsymbol{\Sigma}_1^{-1} (\boldsymbol{\mu}_1 - \boldsymbol{\mu}_0) - k + \ln \frac{|\boldsymbol{\Sigma}_1|}{|\boldsymbol{\Sigma}_0|}\} \end{aligned} \quad (2)$$

where k is a constant, $\mathcal{N}_0 \sim \mathcal{N}(\boldsymbol{\mu}_0, \boldsymbol{\Sigma}_0 = \mathbf{I})$, and \mathbf{I} is the identity matrix. Further, $\mathcal{N}_1 \sim \mathcal{N}(\boldsymbol{\mu}_1, \boldsymbol{\Sigma}_1 = \text{diag}(\sigma_j))$, where σ_j for $j = 1, \dots, D$, for a number of dimensions D , is estimated from the samples of the latent representation. Finally, we assume $\boldsymbol{\mu}_0 = \boldsymbol{\mu}_1$ resulting in the following simplified objective

$$\mathcal{L}_{KL} = D_{KL}(\mathcal{N}_0, \mathcal{N}_1) = \frac{1}{2} \{tr(\boldsymbol{\Sigma}_1^{-1} \boldsymbol{\Sigma}_0) - k + \ln \frac{|\boldsymbol{\Sigma}_1|}{|\boldsymbol{\Sigma}_0|}\}, \quad (3)$$

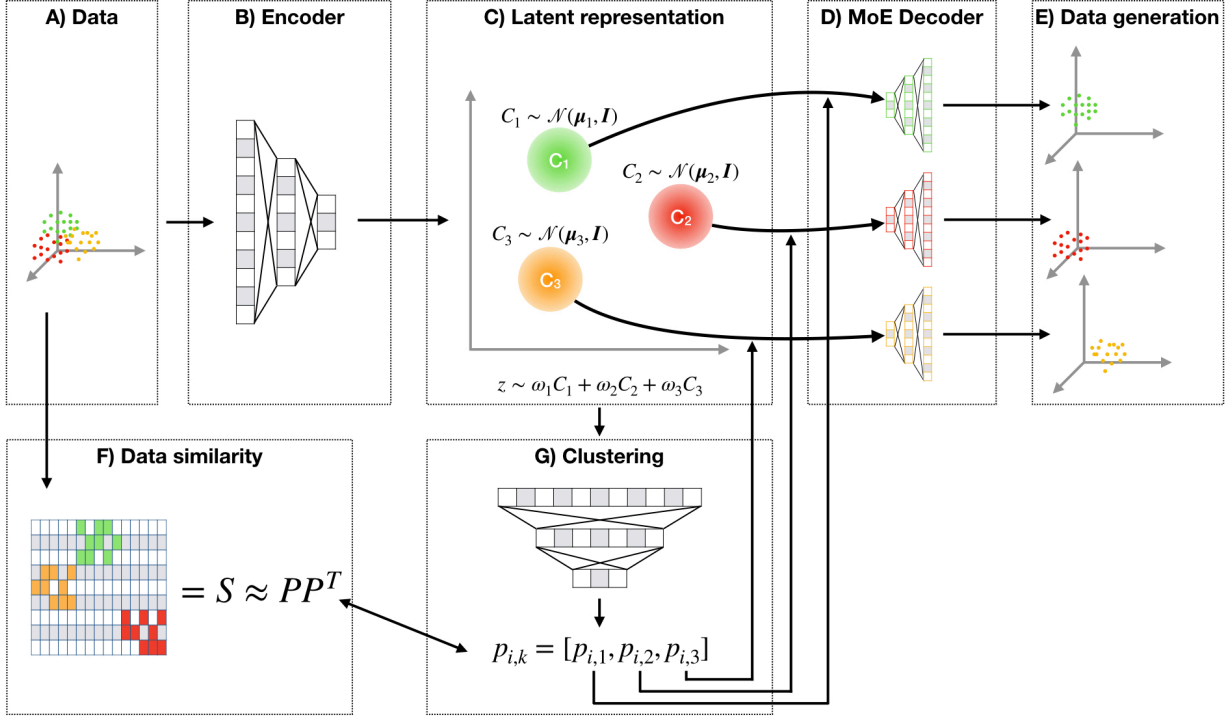


Figure 1: Overview of the proposed model MoE-Sim-VAE. Data (in panel A) gets encoded via an encoder network (B) into a latent representation (C) which is trained to be a mixture of standard Gaussians. Via a clustering network (G), which is trained to reconstruct a user-defined similarity matrix (F), the encoded samples get assigned to the data mode-specific decoder subnetwork (which we call experts) in the MoE Decoder (D). The experts reconstruct the original input data and can be used for data generation when sampling from the variational distribution (E).

to penalize exclusively the covariance of each cluster. It remains to define the reconstruction loss $\mathcal{L}_{reconst}$, where we choose a Binary Cross-Entropy

$$\mathcal{L}_{reconst} = \sum_i^N \sum_d^D x_{i,d} \log(x_{i,d}^{reconst}) \quad (4)$$

between the original data x (scaled between 0 and 1) and the reconstructed data $x^{reconst}$, where i iterates the batch size N and d the dimensions of the data D . Finally the loss for the VAE part is defined by

$$\mathcal{L}_{VAE} = \mathcal{L}_{reconst} + \pi_1 \mathcal{L}_{KL} \quad (5)$$

with a weighting coefficient π_1 which can be optimized as a hyperparameter.

Similarity clustering and gating of latent representation

Training of a data mode-specific generator expert requires samples from the same data mode. This necessitates to solve a clustering problem, that is, mapping the data via the latent representation into K clusters, each corresponding to one of the K generator experts. We solve this clustering problem via a clustering network, also referred to as gating network for MoE models. It takes as input the latent representation z_i of sample i and outputs probabilities $p_{ik} \in [0, 1]$ for clustering sample i into cluster k . According to this cluster assignment, sample i is then gated to expert $k = \operatorname{argmax}_k p_{ik}$ for each sample i . We further define the cluster centers μ_k for $k \in \{1, \dots, K\}$ similar as in the Expectation Maximization (EM) algorithm for Gaussian Mixture models [17] as

$$\mu_k = \frac{1}{N_k} \sum_{i=1}^N p_{ik} z_i, \quad (6)$$

where N_k is the absolute number of data points assigned to cluster k based on highest probability p_{ik} for each sample $i = 1, \dots, N$. The Gaussian mixture distributed latent representation (via KL loss in Equation 3) is motivation for the

empirical computation of the cluster means and further, similar as in the EM algorithm, it allows iterative optimization of the means of the Gaussians. We train the clustering network to reconstruct a data-driven similarity matrix \mathbf{S} , using the Binary Cross-Entropy

$$\mathcal{L}_{Similarity} = \sum_i^N \sum_j^N \mathbf{S}_{i,j} \log((\mathbf{P}\mathbf{P}^T)_{i,j}) \quad (7)$$

to minimize the error in $\mathbf{P}\mathbf{P}^T \approx \mathbf{S}$, with $\mathbf{P} := \{p_{ik}\}_{i \in \{1, \dots, N\}, k \in \{1, \dots, K\}}$ where N is the number of samples (e.g., batch size). Intuitively, $\mathbf{P}\mathbf{P}^T$ approximates the similarity matrix \mathbf{S} since values in $\mathbf{P}\mathbf{P}^T$ are only close to 1 when similar data objects are assigned to the same cluster, similar to the entries in the adjacency similarity matrix \mathbf{S} . This similarity matrix is derived in an unsupervised way in our experiments (e.g. UMAP projection of the data and k-nearest-neighbors or distance thresholding to define the adjacency matrix for the batch), but can also be used to include weakly-supervised information (e.g., knowledge about diseased vs. non-diseased patients). If labels are available, the model could even be used to derive a latent representation with supervision. The similarity feature in MoE-Sim-VAE thus allows to include prior knowledge about the best similarity measure on the data.

Moreover, we apply the DEPICT loss from Dizaji *et al.* [7], to improve the robustness of the clustering. For the DEPICT loss, we additionally propagate a noisy probability \hat{p}_{ik} through the clustering network using dropout after each layer. The goal is to predict the same cluster for both, the noisy \hat{p}_{ik} and the clean probability p_{ik} (without applying dropout). Dizaji *et al.* [7] derived as objective function a standard cross-entropy loss

$$\mathcal{L}_{DEPICT} = -\frac{1}{N} \sum_{i=0}^N \sum_{k=0}^K q_{ik} \log \hat{p}_{ik} \quad (8)$$

whereby q_{ik} is computed via the auxiliary function

$$q_{ik} = \frac{p_{ik} / (\sum_{i'} p_{i'k})^{\frac{1}{2}}}{\sum_{k'} p_{ik'} / (\sum_{i'} p_{i'k'})^{\frac{1}{2}}} . \quad (9)$$

We refer to Dizaji *et al.* [7] for the exact derivation. The DEPICT loss encourages the model to learn invariant features from the latent representation for clustering with respect to noise [7]. Looking at it from a different perspective, the loss helps to define a latent representation which has those invariant features to be able to reconstruct the similarity and therefore the clustering correctly. The complete clustering loss function $\mathcal{L}_{Clustering}$ is then defined by

$$\mathcal{L}_{Clustering} = \mathcal{L}_{Similarity} + \pi_2 \mathcal{L}_{DEPICT} \quad (10)$$

with a mixture coefficient π_2 which can be optimized as a hyperparameter.

MoE-Sim-VAE loss function

Finally, the MoE-Sim-VAE model loss is defined by

$$\mathcal{L}_{MoE-Sim-VAE} = \underbrace{\mathcal{L}_{VAE}}_{\mathcal{L}_{reconst} + \pi_1 \mathcal{L}_{KL}} + \underbrace{\mathcal{L}_{Clustering}}_{\mathcal{L}_{Similarity} + \pi_2 \mathcal{L}_{DEPICT}} \quad (11)$$

which consists of the two main loss functions \mathcal{L}_{VAE} , acting as a regularization for the latent representation, and $\mathcal{L}_{Clustering}$, which helps to learn the mixture components based on an *a priori* defined data similarity. The model objective function $\mathcal{L}_{MoE-Sim-VAE}$ can then be optimized end-to-end to train all parts of the model.

Results

In the following we report superior clustering and generating results of MoE-Sim-VAE on real world problems. First, we evaluate MoE-Sim-VAE on images from MNIST and show why a MoE decoder is beneficial. Second, we present significantly better clustering results on mouse organ single-cell RNA sequencing data. Third, we apply MoE-Sim-VAE to cluster cell types in Peripheral Blood Mononuclear Cells using CyTOF measurements on 272 distinct data sets significantly better than competitors. (Exact model and optimization details for all experiments can be found in Supporting Information Section B)

Table 1: Performance comparison of our method MoE-Sim-VAE with several published methods on MNIST. The Table is mainly extracted from [1] and complemented with results of interest. (“-”: metric not reported)

Method	NMI	ACC
JULE [25]	0.915	-
CCNN [26]	0.876	-
DEC [27]	0.80	0.843
DBC [28]	0.917	0.964
DEPICT [7]	0.916	0.965
DCN [19]	0.81	0.83
Neural Clustering [29]	-	0.966
UMMC [30]	0.864	-
VaDE [2]	0.876	0.945
TAGnet [31]	0.651	0.692
IMSAT [32]	-	0.984
Aljalbout <i>et al.</i> [1]	0.923	0.961
MIXAE [21]	-	0.945
Spectral clustering [34]	0.754	0.717
SpectralNet [34]	0.924	0.971
<i>MoE-Sim-VAE</i> (proposed)	0.935	0.975

Unsupervised clustering, representation learning and data generation on MNIST

We trained a MoE-Sim-VAE model on images from MNIST. We compared our model against multiple models which were recently reviewed in Aljalbout *et al.* [1], and specifically against VaDE [2] which shares similar properties with MoE-Sim-VAE. The VaDE model is comprising a mixture of Gaussians as underlying distribution in the latent representation of a Variational Autoencoder (more detailed comparison in Supporting Information Section B.2).

We compare the models with the Normalized Mutual Information (NMI) criterion but also classification accuracy (ACC) (Table 1). The MoE-Sim-VAE outperforms the other methods w.r.t. clustering performance when comparing NMI and achieves the second-best result when comparing ACC. Note that for comparability reasons we used the number of experts $k = 10$ in our model to fit the existing number of digits in MNIST. To prove that MoE-Sim-VAE is able to learn the correct number of experts, we report in Supporting Information Section B.1 a study on synthetic data.

We use a UMAP projection [3] of MNIST as our similarity measure and then apply k-nearest-neighbors of each sample in a batch. In an ablation study, we show the importance of the similarity matrix to create a clear separation of the different digits in the latent representation. Therefore, we computed a test statistic based on the Maximum Mean Discrepancy (MMD) [14, 15] which can be used to test if two samples are drawn from the same distribution (see Supporting Information Section A.2). In this work we use MMD to test if samples of different clusters of the latent representation are similar. When sampling twice from the same cluster we get an average MMD test statistic of $t_{\text{sim}} = -0.05$ with, and $t = -0.11$ without similarity matrix, whereas the average distance between samples from two different clusters is significantly larger when training with similarity matrix $t_{\text{sim}} = 221.66$ compared to when training without $t = 49.29$. This clearly suggests better separation on the latent representations between the clusters when being able to define a respective similarity (Supporting Information Figure B.2).

In addition to the clustering network, we can make use of the latent representation for image generation purposes. The latent representation is trained as a mixture of standard Gaussians. The means of these Gaussians are the centers of the clusters trained via the clustering network. Therefore, the variational distribution can be sampled from and gated to the cluster-specific expert in the MoE-decoder. The expert then generates new data points for the specific data mode. Results and the schematic are displayed in Figure 2.

In an ablation study, we compare the two models MoE-Sim-VAE and VaDE [2] on generating MNIST images with the request for a specific digit. The goal is to show that a MoE decoder, as proposed in our model, is beneficial. We focus our comparison to VaDE since this model, as the MoE-Sim-VAE, resorts to a mixture of Gaussian latent representation but differs in generating images by means of a single decoder network instead of a Mixture-of-Expert decoder network. The rationale for our design choice is to ensure that smaller sub-networks learn to reproduce and generate specific modes of the data, in this case of specific MNIST digits.

To show that both models’ latent representations are separating the different clusters well, we computed the Maximum Mean Discrepancy (MMD) [14], similar as introduced above. An MMD statistic of $t_{\text{MoE-Sim-VAE}} = 256.31$ and

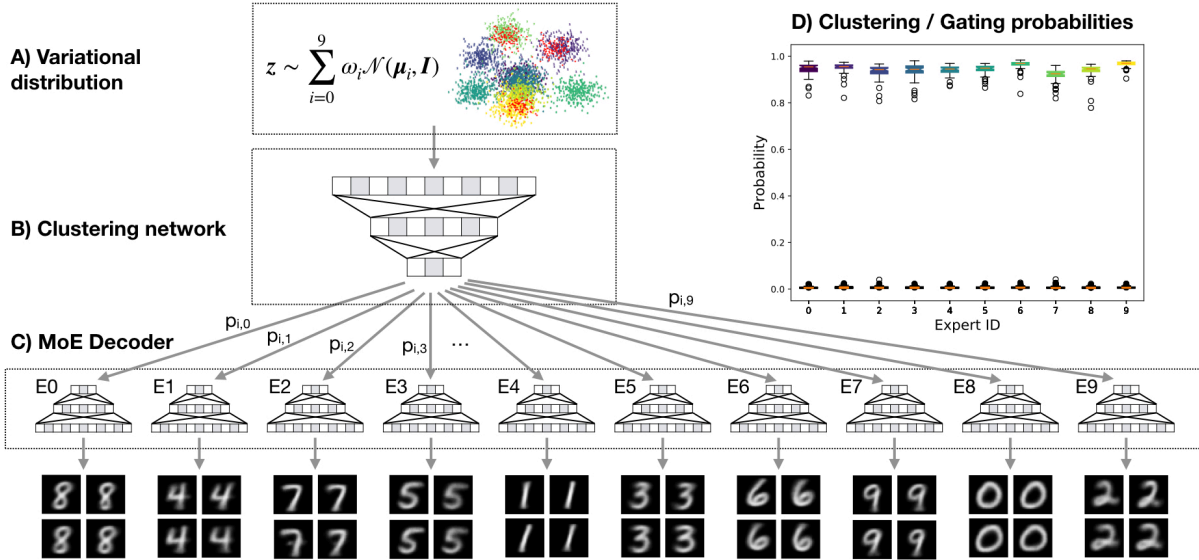


Figure 2: Generation of MNIST digit images. Data points from the latent representation (A) which is learned to be a mixture of standard Gaussians and then clustered and gated (B) to the data-mode-specific experts of the MoE Decoder (C). (D) All samples from the variational distribution were correctly classified and therefore also correctly gated.

$t_{\text{VaDE}} = 355.14$ suggests separation of the clusters when sampling in the latent representations of both models. Therefore, both latent representations can separate the clusters of respective digits well, such that the decoder gets well-defined samples to generate the requested digit. Hence, the main difference of generating specific digits arises in the decoder/generator networks (Supporting Information Figure B.3).

We evaluated the importance of the MoE-Decoder to (1) accurately generate requested digits and (2) be efficient in generating requested digits. Specifically, we sampled 10,000 points from each mixture component in the latent representation, generated images, and used the model’s internal clustering to assign a probability to which digits were generated. To generate correct and high-quality images with VaDE, the posterior of the latent representation needs to be evaluated for each sample. This was done for the different thresholds $\phi \in [0.0, 0.1, 0.2, \dots, 0.9, 0.999]$. The default threshold [2] used was $\phi = 0.999$. To compare the separation of the clusters in the latent representation above using MMD, we used a threshold of only $\phi = 0.8$, which already is enough to have higher separation based on MMD. Instead of thresholding the latent representation, we ran the generation process for MoE-Sim-VAE for each threshold with the same settings. To generate images from VaDE we used the Python implementation (<https://github.com/slim1017/VaDE>) and model weights publicly available from Jiang *et al.* [2].

As a result the MoE-Sim-VAE generates digits more accurately with fewer resources required, especially when comparing the number of iterations required to fulfill the default posterior threshold of 0.999. VaDE needs nearly 2 million iterations to find samples that fulfill the aforementioned threshold criterion whereas the MoE-Sim-VAE only requires 10,000 for a comparable sample accuracy. In comparison, the mean accuracy over all thresholds for MoE-Sim-VAE is 0.970, whereas VaDE reaches on average only 0.944 (Supporting Information Figure B.4, B.5, B.6).

Clustering organ-specific single cell RNA-seq data

Single-cell RNA-sequencing (scRNA-seq) measurements allow measuring transcriptomes of tens of thousands of single cells. Clustering of the resulting data into groups representing biological phenotypes, such as cell type or tissue type, constitutes a major analysis task in scRNA-seq studies. In the following, we present how MoE-Sim-VAE outperforms the methods Gaussian Mixture Models (GMM), k-means, hierarchical clustering, HDBSCAN, fuzzy-c-means (FCM) and Louvain [40, 41, 42] for clustering the scRNA-seq data of the Tabula Muris study covering seven different mouse organs [36].

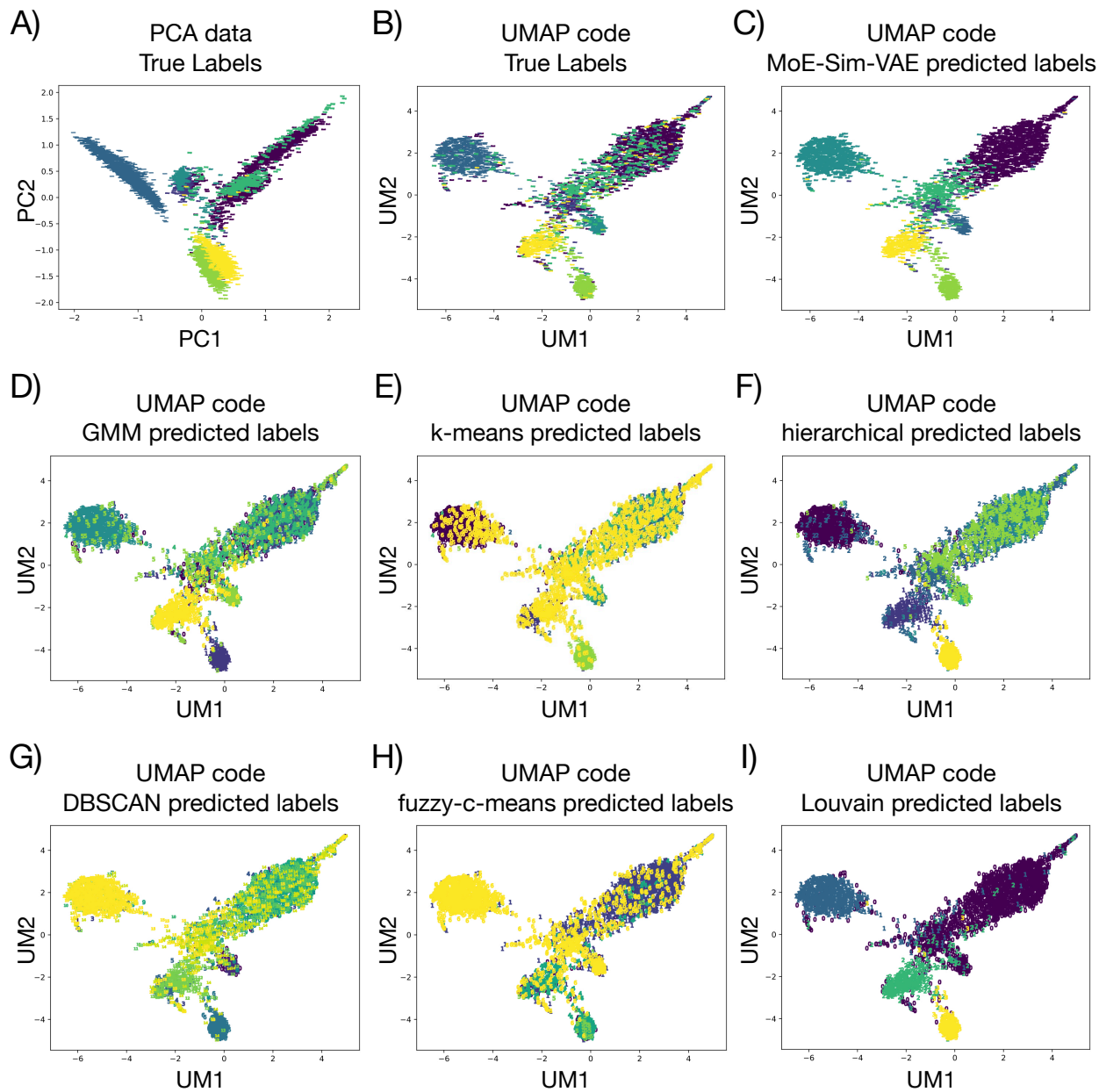


Figure 3: Comparison of clustering results. A) Principal Component Analysis of the original data with true labels. The remaining panels are UMAP representations of the latent representation inferred from MoE-Sim-VAE with B) true labels. C) predicted labels from MoE-Sim-VAE. D) predicted labels from Gaussian Mixture Model. E) predicted labels from k-means. F) predicted labels from hierarchical clustering. G) predicted labels from DBSCAN. H) predicted labels from fuzzy-c-means. I) predicted labels from Louvain.

Table 2: Results on clustering mouse organs based on RNA-seq. We compare MoE-Sim-VAE to the competitor methods Gaussian Mixture Models (GMM), k-means, Hierarchical clustering, DBSCAN, FCM and Louvain clustering.

Method	F-measure	NMI
GMM PCA k = 20	0.632	0.487
k-means PCA k = 40	0.606	0.443
hierarchical PCA k = 20	0.643	0.534
HDBSCAN PCA k = 50	0.615	0.517
fuzzy-c-means PCA k = 50 m=4	0.549	0.336
Louvain PCA k = 30 resolution = 0.01	0.679	0.584
<i>MoE-Sim-VAE</i> (proposed)	0.748	0.519

MoE-Sim-VAE allows for incorporation of a user defined similarity and therefore also prior knowledge about the data. From literature we identified for each organ a representing signature gene and use each to encode prior expectation of organ assignment for each cell measurement. Namely, we take advantage of the high expressions of *Lpl* in the heart, *Miox* in kidney, *Hpx* in liver, *Tspan1* in large intestine, *Prx* in lung, *Cd79a* in spleen and *Dntt* in thymus [39, 38, 43, 37]. Single cells which show above average expression of a respective signature gene are considered to be similar. For the training of MoE-Sim-VAE we only considered cells which show above average expression in exactly one of the respective organ-specific signature genes (does not apply for the test data).

MoE-Sim-VAE outperforms all above mentioned baseline approaches in clustering the single cells with respect to the organ of origin. Our model reaches a F-measure (Supporting Information Section A.1) of 0.748 and is therefore close to 0.1 better compared to the second best competitor. We performed a hyperparameter screening for the competitor methods (more details in Supporting Information Section B.3) and chose the best results achieved on the test dataset based on the F-measure as well. In Table 2 we present the exact results in detailed comparison. In Figure 3A-B) we show a Principal Component Analysis (PCA) of the original data as well as of the latent representation of MoE-Sim-VAE. It can be seen that the organs are better separated in the latent representation inferred from our model which enables for better clustering results of MoE-Sim-VAE (Figure 3C)). In Figure 3D-I) we present the results of the competitor methods in the latent representation of MoE-Sim-VAE and can clearly see that Louvain performs second best, but poorly separates cells from organs which are close to each other or overlap in the original PCA representation.

Learning cell type composition in peripheral blood mononuclear cells using CyTOF measurements

In the following, we want to assess representation learning performance on the real-world problem of cell type definition from single-cell measurements. Cytometry by time-of-flight mass spectrometry (CyTOF) is a state-of-the-art technique allowing measurements of up to 1,000 cells per second and in parallel over 40 different protein markers of the cells [18]. Defining biologically relevant cell subpopulations by clustering this data is a common learning task [4, 5].

Many methods have been developed to tackle the problem introduced above and were compared on four publicly available datasets in Weber and Robinson [5]. The best out of 18 methods were FlowSOM [8], PhenoGraph [10] and X-shift [9]. These are based on k-nearest-neighbors heuristics, either defined from a spanning graph or from estimating the data density. In contrast to these methods, MoE-Sim-VAE can map new cells into the latent representation, assign probabilities for cell types, and infer an interpretable latent representation, allowing intuitive downstream analysis by domain experts.

We applied MoE-Sim-VAE to the same datasets as in Weber and Robinson [5] and achieve superior results in classification using the F-measure [4] in three out of four datasets. Similarly as in Weber and Robinson [5], we trained MoE-Sim-VAE 30 times and report in Table 3 (adopted from Weber and Robinson [5]) the means and standard deviation across all runs (Supporting Information Figure B.7). As a MoE-Sim-VAE similarity measure we used a UMAP projection with Canberra distance [44] as metric and computed similarly to the MNIST experiments the k-nearest-neighbors of each sample in the batch. This applies for all CyTOF experiments.

Table 3: Comparison of MoE-Sim-VAE performance to competitor methods in defining cell type composition in CyTOF measurements. The results in the table are extracted from the review paper of [5], where 18 methods are compared on four different datasets. Our model outperforms the baselines on three out of four data sets.

Method	Levine_32dim	Levine_13dim	Samusik_01	Samusik_all
ACCENSE	0.494	0.358	0.517	0.502
ClusterX	0.682	0.474	0.571	0.603
DensVM	0.66	0.448	0.239	0.496
FLOCK	0.727	0.379	0.608	0.631
flowClust	N/A	0.416	0.612	0.61
flowMeans	0.769	0.518	0.625	0.653
flowMerge	N/A	0.247	0.452	0.341
flowPeaks	0.237	0.215	0.058	0.323
FlowSOM	0.78	0.495	0.707	0.702
FlowSOM_pre	0.502	0.422	0.583	0.528
immunoClust	0.413	0.308	0.552	0.523
k-means	0.42	0.435	0.65	0.59
PhenoGraph	0.563	0.468	0.671	0.653
Rclusterpp	0.605	0.465	0.637	0.613
SamSPECTRAL	0.512	0.253	0.263	0.138
SPADE	N/A	0.127	0.169	0.13
SWIFT	0.177	0.179	0.202	0.208
X-Shift	0.691	0.47	0.679	0.657
<i>MoE-Sim-VAE</i> (proposed)	0.70 ± 0.04	0.68 ± 0.01	0.76 ± 0.03	0.74 ± 0.02

Further, we trained a MoE-Sim-VAE model with a fixed number of experts $k = 15$ (thereby slightly overestimating the true number of subpopulations) on 268 datasets from Bodenmiller *et al.* [11] and achieve superior clustering results of cell subpopulations in the data when comparing to state-of-the-art methods in this field (PhenoGraph, X-Shift, FlowSOM). Results are summarized in Figure 4 as well as exactly listed in Supporting Information Table A1.

Discussion

Our MoE-Sim-VAE model can infer similarity-based representations, perform clustering tasks, and efficiently as well as accurately generate high-dimensional data. The training of the model is performed by optimizing a joint objective function consisting of data reconstruction, clustering, and KL loss, where the latter regularizes the latent representation. On the benchmark dataset of MNIST, we present superior clustering performance and the efficiency and accuracy of MoE-Sim-VAE in generating high-dimensional data. On the biological real-world tasks of clustering mouse organs and defining cell subpopulations in complex single-cell data, we show superior performances compared to state-of-the-art methods on a vast range of over 270 datasets and therefore demonstrate the MoE-Sim-VAE’s real-world usefulness.

Future work might include to add adversarial training to the MoE decoder, which could improve image generation to create even more realistic images. Also, specific applications might benefit from replacing the Gaussian with a different mixture model. Especially biological data is not always generated from Gaussian distributions. So far the MoE-Sim-VAE’s similarity measure has to be defined by the user. Relaxing this requirement and allowing for learning a useful similarity measure automatically for inferring latent representations will be an interesting extension to explore. This could be useful in a weakly-supervised setting, which often occurs for example in clinical data consisting of healthy and diseased patients. Minor details between a healthy and diseased patient might make a huge difference and could be learned from the data using neural networks.

In summary, we expect the MoE-VAE model, as well its future extensions, to be a valuable contribution to the computational biology toolbox to identify biological group structure in high-dimensional molecular data modalities under consideration of weak prior knowledge, in particular including single-cell omics data.

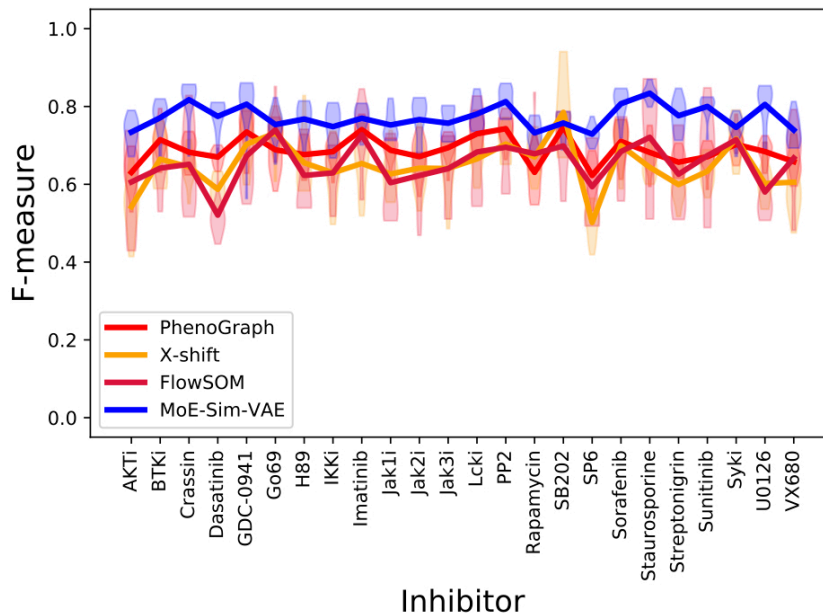


Figure 4: Comparison of MoE-Sim-VAE to the most popular competitor methods on defining cell types in peripheral blood mononuclear cell data via CyTOF measurements. On the x-axis different inhibitor treatments are listed whereas the y-axis reports the respective F-measure. Each violin plot represents a run on a different inhibitor with multiple wells, whereas the line connects the means of the performance on the specific inhibitor.

Acknowledgments

AK was supported by the "SystemsX.ch HDL-X" and "ERASysApp Rootbook" and the PHRT grant #2017-103. AK wants to thank Florian Buettner for helpful discussions and his inspirational attitude. VF is supported by a PhD fellowship from the Swiss Data Science Center and by the PHRT grant #2017-110 of the ETH Domain.

Supporting Information

Mixture-of-Experts Variational Autoencoder for Clustering and Generating from Similarity-Based Representations on Single Cell Data

A Metrics

A.1 F-measure

We compare results based on F-measure [4], which is defined as follows

$$F(C, K) = \sum_{c_i \in C} \frac{|c_i|}{N} \max_{k_j \in K} \{F(c_i, k_j)\} \quad (12)$$

where N is the number of samples $C = \{c_1, c_2, \dots, c_n\}$ and $K = \{k_1, k_2, \dots, k_m\}$ are the cluster result and the reference cluster, respectively. Further $F(c_i, k_j)$ is the harmonic mean of precision and recall according to

$$F(c_i, k_j) = \frac{2Pr(c_i, k_j)Re(c_i, k_j)}{Pr(c_i, k_j) + Re(c_i, k_j)} \quad (13)$$

whereby $Pr(c_i, k_j)$ is the precision and $Re(c_i, k_j)$ is the recall.

A.2 Maximum Mean Discrepancy

One estimator of the Maximum Mean Discrepancy (MMD) [14] is defined as

$$\begin{aligned} \widehat{MMD}^2(X, Y) = t = & \frac{1}{\binom{m}{2}} \sum_{i \neq i'} k(X_i, X_{i'}) + \\ & \frac{1}{\binom{m}{2}} \sum_{j \neq j'} k(Y_j, Y_{j'}) - \\ & \frac{2}{\binom{m}{2}} \sum_{i, j} k(X_i, Y_j) \end{aligned} \quad (14)$$

where $X = \{\hat{x}_1, \dots, \hat{x}_m\} \stackrel{iid}{\sim} P$, $Y = \{\hat{y}_1, \dots, \hat{y}_m\} \stackrel{iid}{\sim} Q$ are samples from two distributions (e.g. samples from two different clusters of the latent representation, for MNIST of two different digits) and k is a kernel function, where we use the popular RBF kernel. Based on that estimator Sutherland *et al.* [15] introduced the hypothesis test

$$H_0 : P = Q \quad (15)$$

$$H_1 : P \neq Q \quad (16)$$

using the statistic $\widehat{MMD}^2(X, Y)$. The distribution for P and Q is not required to be known. Sutherland *et al.* [15] used MMD and this test to train a Generative Adversarial Network (GAN) and also to evaluate the generative performance of the model. In this work we use $\widehat{MMD}^2(X, Y)$ to test if samples of different clusters of the latent representation are similar, or in other words the distance of the distributions. We used the Python implementation (https://github.com/dougalsutherland/opt-mmd/blob/master/two_sample/mmd_test.py) from Sutherland *et al.* [15].

B Results

B.1 Evaluation of MoE-Sim-VAE on synthetic data

We evaluated MoE-Sim-VAE on synthetic data sampled from a Gaussian mixture distribution with randomly sampled parameters. Figure B.1 depicts the results and shows that MoE-Sim-VAE can identify the correct number of clusters up to 23 mixture components. The Encoder and Decoder networks are dense layers stacked with depth parameters listed below. Further model and training details:

- number of experts: $\{2, \dots, 40\}$

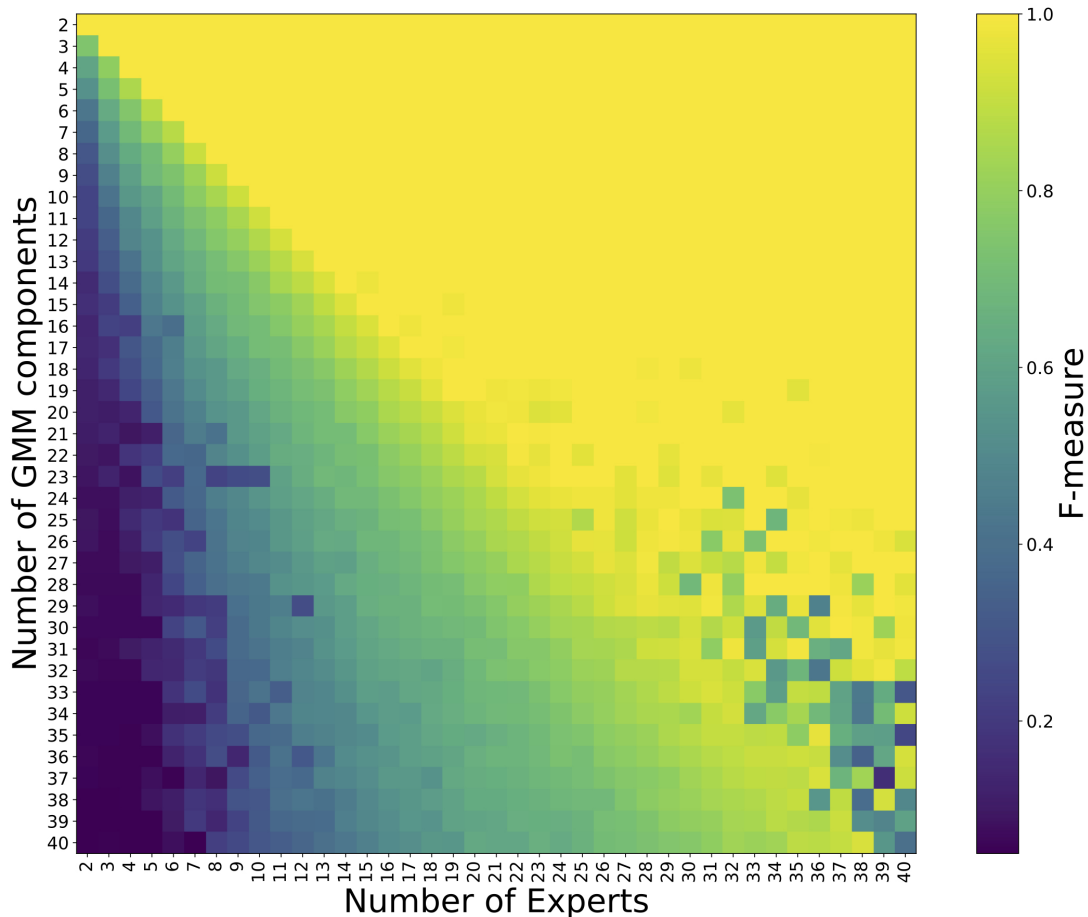


Figure B.1: Testing MoE-Sim-VAE on data sampled from a Gaussian mixture model with randomly sampled parameters. We tested for specific number of synthetic mixture components and iterating number of experts. Until a number of GMM components of 23 MoE-Sim-VAE is precise in learning the real number of clusters even when allowing the model to have 40 experts.

- batch size: 512
- code size: 10
- Number of iterations: 5000
- activation function; elu
- loss coefficient data reconstruction: 0.487
- loss coefficient clustering : 0.487
- loss coefficient mixture of Gaussian: 0.024
- learning rate: 0.001
- batch normalization
- dropout rate: 0.5
- distance threshold (perplexity parameter): 2
- encoder depth: 3
- encoder internal size: 50
- decoder depth: 3
- decoder internal size: 50

- depth clustering network: 5
- internal size clustering network: 100
- trainable parameters: depending on number of experts

B.2 Unsupervised clustering, representation learning and data generation on MNIST

Jiang *et al.* [2] introduced the VaDE model, comprising a mixture of Gaussians as underlying distribution in the latent representation of a Variational Autoencoder. Optimizing the Evidence Lower Bound (ELBO) of the log-likelihood of the data can be rewritten to optimize the reconstruction loss of the data and KL divergence between the variational posterior and the mixture of Gaussians prior. Jiang *et al.* [2] motivate the use of two separate networks for reconstruction and the generation process of the model. Further, to effectively generate images from a specific data mode and to increase image quality, the sampled points have to surpass a certain posterior threshold and are otherwise rejected. This leads to an increased computational effort. The MoE Decoder of our model, which is used for both reconstruction and generation, does not need such a threshold.

In the following we define the architecture of MoE-Sim-VAE. The Encoder architecture:

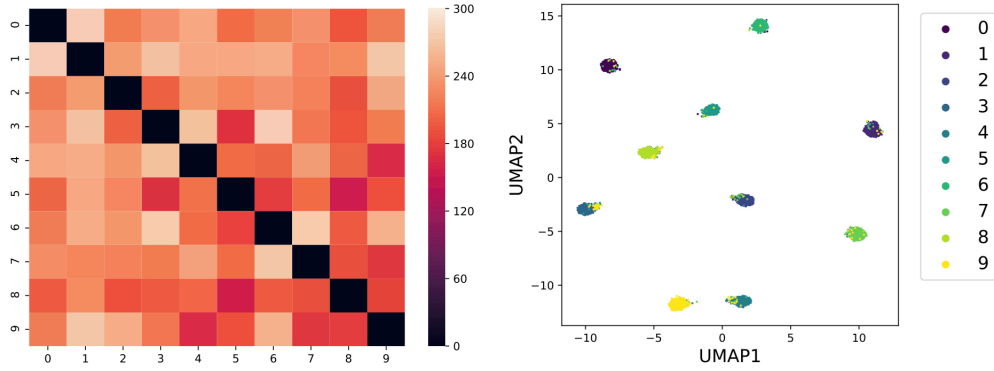
- Convolution layer (filters 64, 3x3, elu activation)
- batch normalization
- Convolution layer (filters 128, 3x3, elu activation)
- batch normalization
- Max Pooling (2x2)
- batch normalization
- Convolution layer (filters 128, 3x3, elu activation)
- batch normalization
- Max Pooling (2x2)
- batch normalization
- Convolution layer (filters 64, 3x3, elu activation)
- Batch normalization
- Convolution layer (filters 8, 3x3, elu activation)
- Batch normalization
- Dense layer (code size)

Architecture of a Decoder expert:

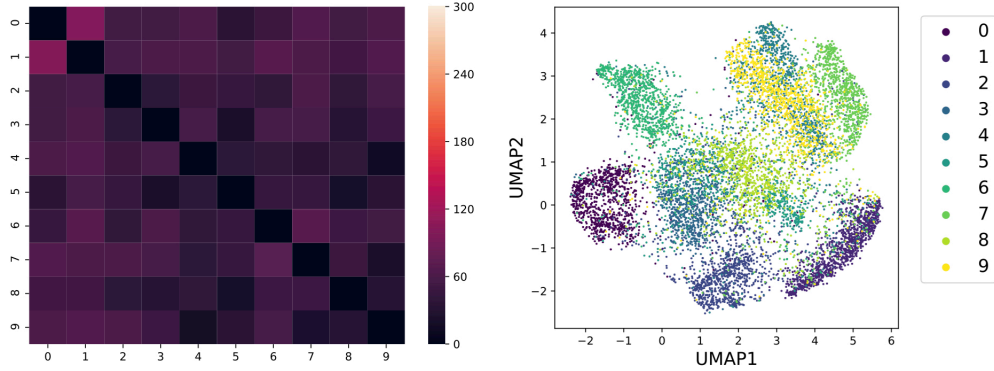
- Dense layer (size=7x7x8)
- Convolution layer (filters 128, 3x3, elu activation)
- Upsampling layer (2x2)
- Convolution layer (filters 64, 3x3, elu activation)
- Upsampling layer (2x2)
- Convolution layer (filters 32, 3x3, elu activation)
- Convolution layer (filters 1, 3x3, elu activation)

Model and training details:

- number of experts: 10
- batch size: 128
- code size: 68
- Number of iterations: 20000
- activation function; elu
- loss coefficient data reconstruction: 0.487



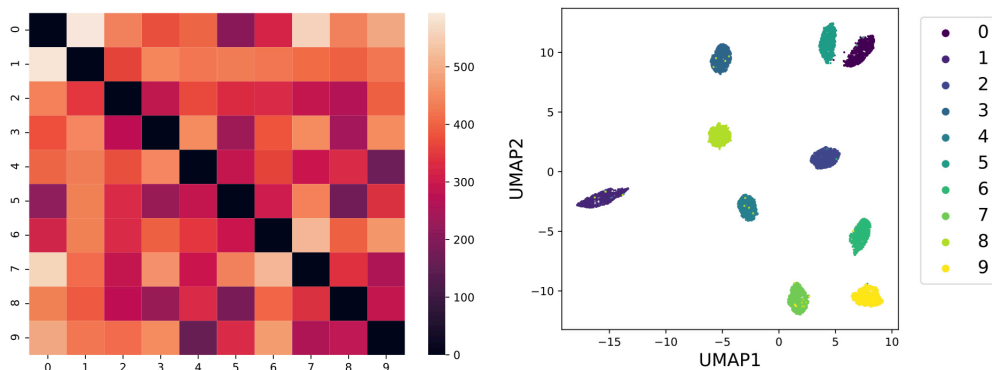
(a)



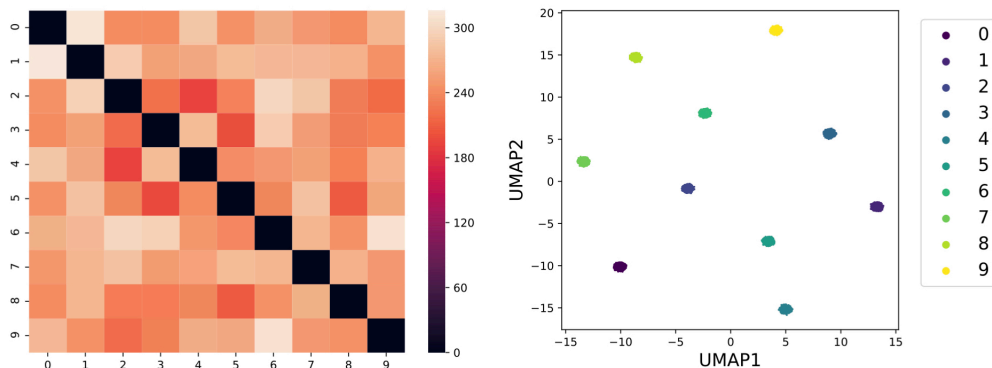
(b)

Figure B.2: Ablation study on the similarity matrix S . Both figures show the MMD statistic and UMAP [3] projection of reconstructed MNIST digits computed on the latent representation. Figure B.2a shows the results on MoE-Sim-VAE trained with the similarity matrix. The different digits separate well which can also be seen in the heatmap showing the MMD statistics between all digits. In comparison, Figure B.2b shows results of the MoE-Sim-VAE model ignoring the similarity matrix setting the loss coefficient to zero. One can observe that the MMD statistic, which can be seen as a similarity measure of two distributions, is way lower compared to the model including the similarity matrix. Further, also the UMAP projection confirms less separation in the latent representation between the different digits.

- loss coefficient clustering : 0.487
- loss coefficient mixture of Gaussian: 0.024
- learning rate: 0.0001
- batch normalization
- dropout rate: 0.5
- k from kNN (perplexity parameter): 10
- depth clustering network: 3
- internal size clustering network: 200
- trainable parameters: 1619446

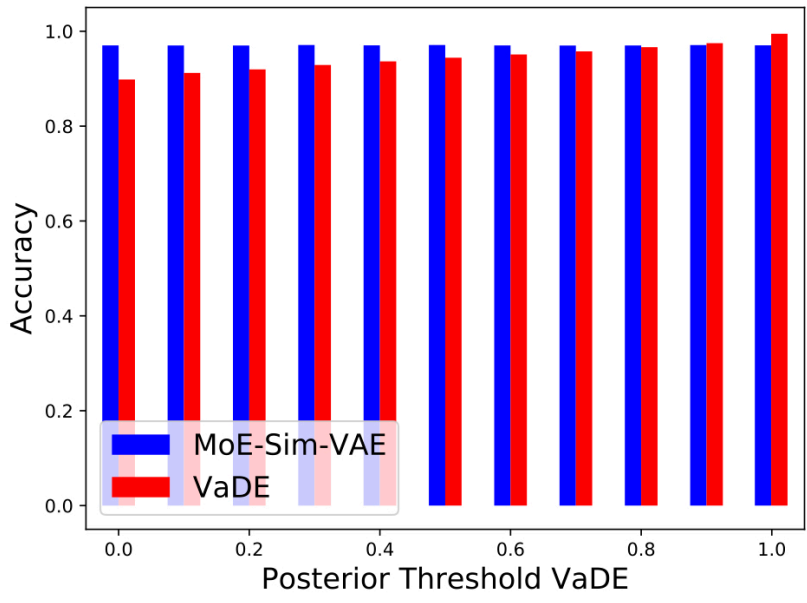


(a)

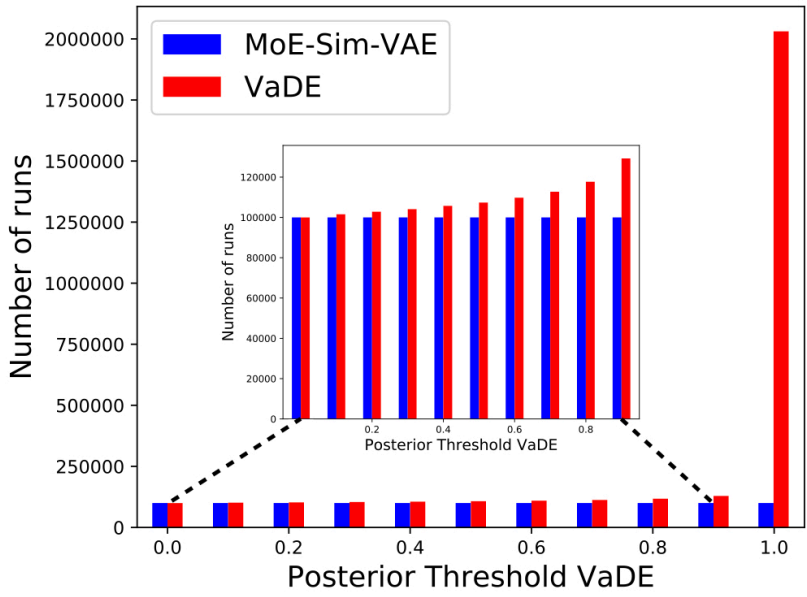


(b)

Figure B.3: Comparison of two sample MMD test [15] on the distributions from the different mixture components in the latent representation. The heatmaps on the left side show the estimation of the MMD which can be seen as the distance between pairs of distributions. The figures on the right side show the separation of the cluster in the latent representation based on a dimensionality reduction via UMAP [3]. Figure B.3a shows the results for the clusters of VaDE at a posterior threshold of 0.8 which is the first threshold which shows total separation of all clusters. Figure B.3b shows the separation of the clusters in latent space learned from MoE-Sim-VAE. For both methods, all distributions belonging to clusters of different respective digits show a larger distance compared to the diagonal of matching distributions, such that we generate images from a well-separated latent representation for both methods and therefore the main difference comes from the decoders.



(a)



(b)

Figure B.4: Comparison of data generation process between Moe-Sim-VAE and VaDE [2]. Figure B.4a shows the accuracy of how certain a specific digit can be generated from the respective cluster in the latent representation whereas Figure B.4b compares the number of runs until a sample from the latent representation satisfied the posterior criterion from VaDE. It needs to be mentioned that MoE-Sim-VAE does not require any thresholding such that we ran the data generation process multiple times with the same settings to compare with VaDE. In total 10000 samples are generated for each digit.

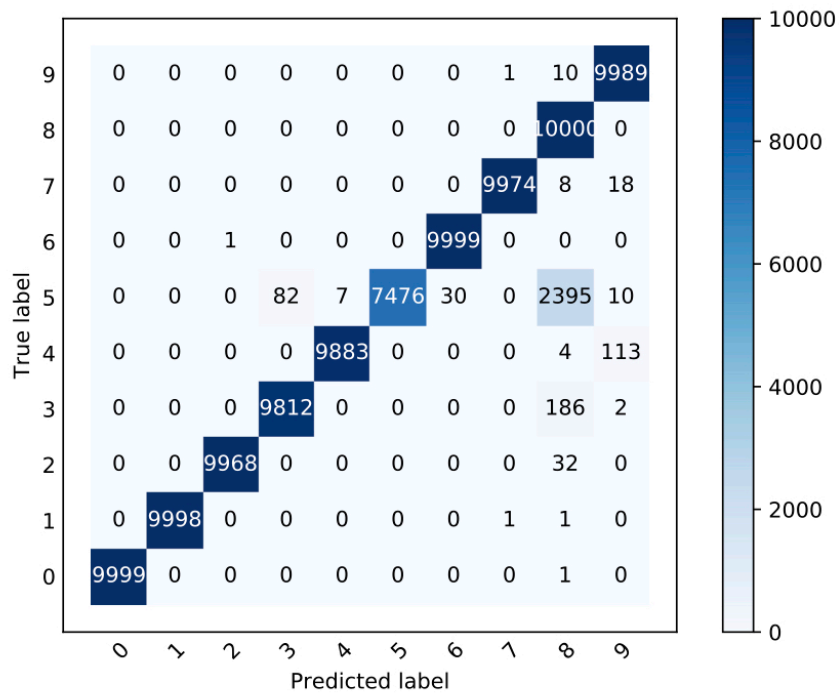
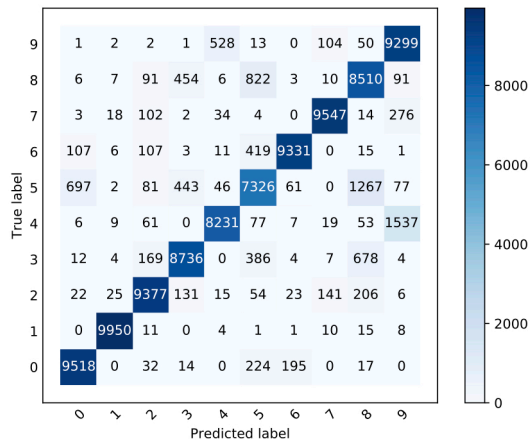
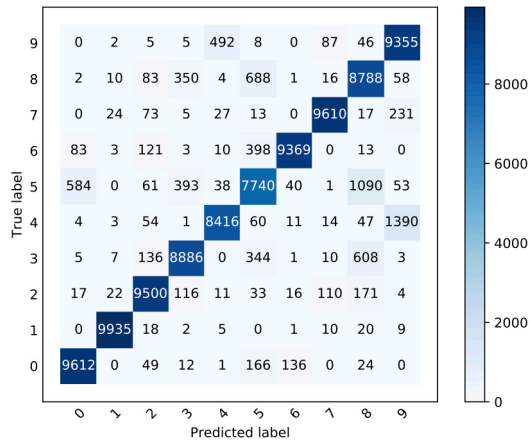


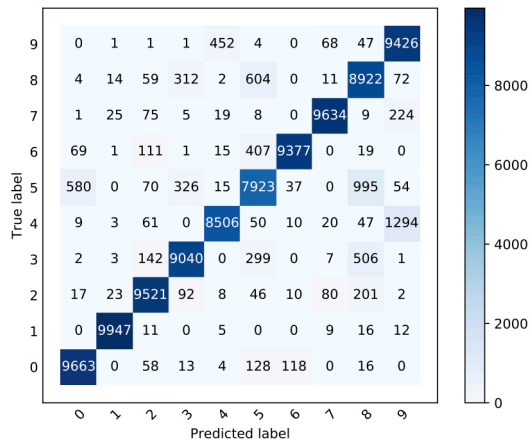
Figure B.5: Confusion map for data generation using MoE-Sim-VAE. Besides the systematic error of confusing digit 5 and 8, which can also depend on the clustering network, the digit generation of our model performs very precise with a high accuracy of generating the digit asked for. In comparison to VaDE [2] our model does not need any threshold on samples from the latent representation which reduces the computational costs by far.



(a)



(b)



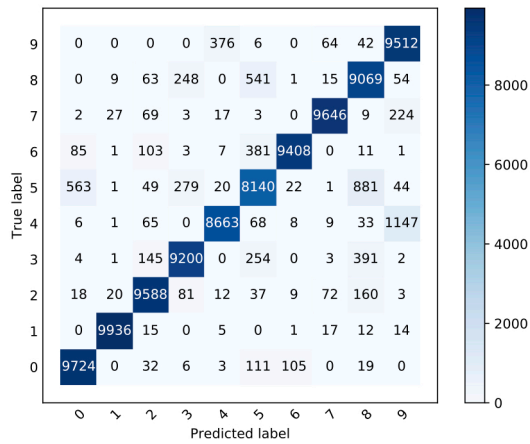
(c)

Figure B.6: Confusion maps for data generation using VaDE.

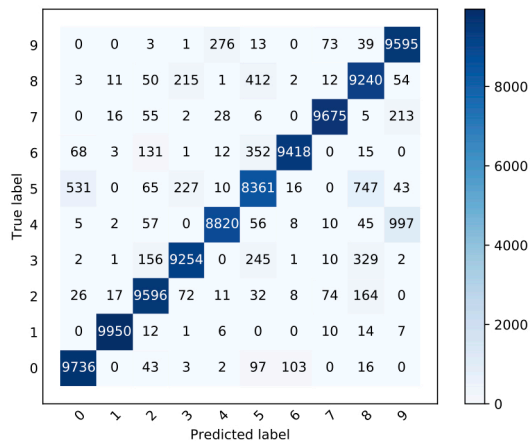
Figure B.6a Posterior threshold 0.0.

Figure B.6b Posterior threshold 0.1.

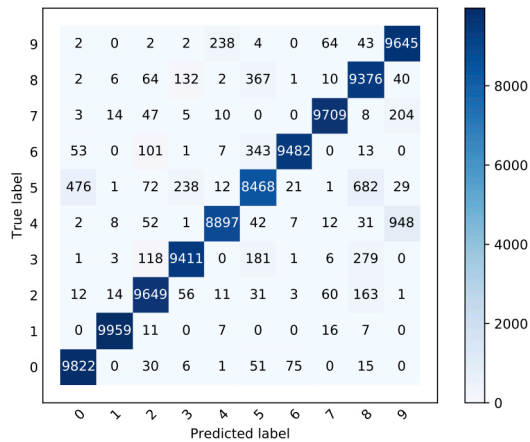
Figure B.6c Posterior threshold 0.2.



(d)



(e)



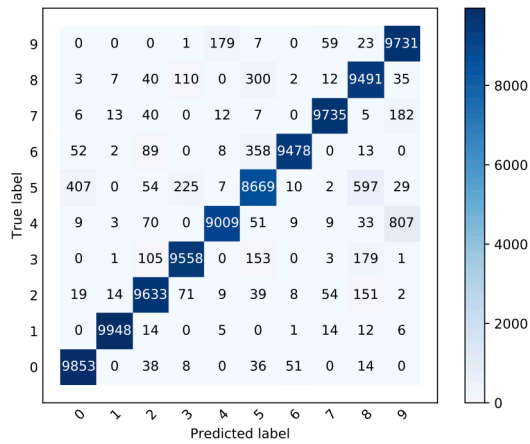
(f)

Figure B.6: Confusion maps for data generation using VaDE.

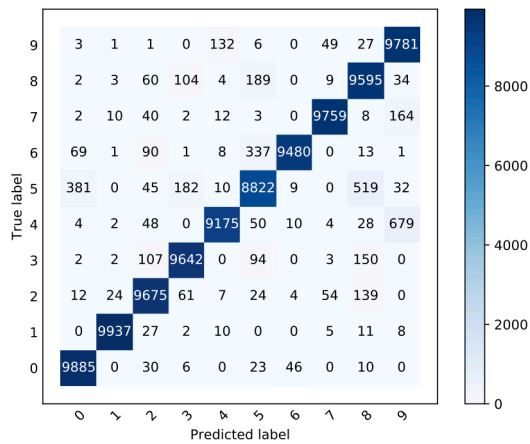
Figure B.6d Posterior threshold 0.3.

Figure B.6e Posterior threshold 0.4.

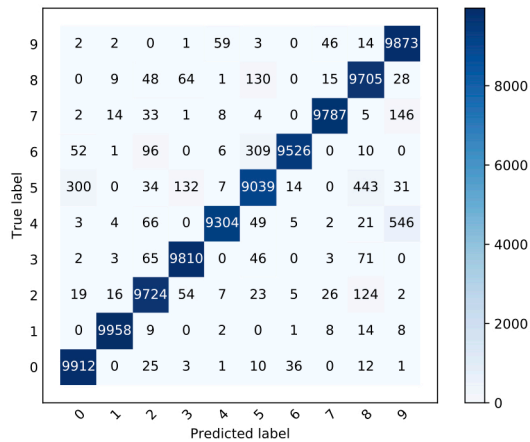
Figure B.6f Posterior threshold 0.5.



(g)



(h)



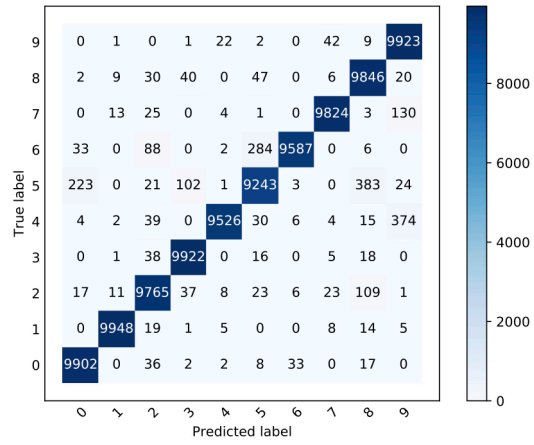
(i)

Figure B.6: Confusion maps for data generation using VaDE.

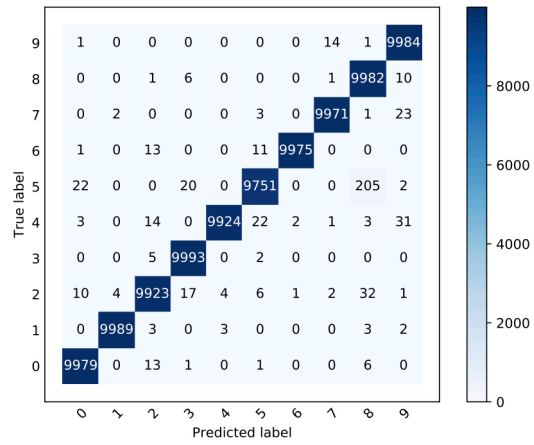
Figure B.6g Posterior threshold 0.6.

Figure B.6h Posterior threshold 0.7.

Figure B.6i Posterior threshold 0.8.



(j)



(k)

Figure B.6: Confusion maps for data generation using VaDE.

Figure B.6j Posterior threshold 0.9.

Figure B.6k Posterior threshold 0.999. (default for VaDE [2])

B.3 Clustering organ-specific single cell RNA-seq data

In all our experiments we filtered the data for genes with low total sum and low variance in expression. Therefore, we used the 20 percent lower quantile and ignored genes which fall underneath this threshold.

All competitor methods were applied on the first k principal components of the scRNA-seq measurements. For a fair comparison we screened the number of principal components ($k \in [10, 20, \dots, 100]$) and for Louvain clustering (resolution), HDBSCAN (minimum cluster size) and fuzzy-c-means (exponent for the fuzzy partition matrix) additional hyperparameter were tuned via grid search. HDBSCAN returns cells which are assigned to noise and not to one of the clusters. For fair comparison on the test dataset we assigned the noise cells to the nearest cluster centroid. All methods were applied on either principal components of the counts itself or of Transcripts Per Million (TPM) normalized count data. Additionally, the methods were screened on 0-1 scaled data, which provided the better results compared to unscaled data. The best results based on F-measure, defined in Equation 12, were chosen.

The encoder and decoder networks are stacked dense layers with batch normalization and activation after each layer level. The clustering network is a stacked dense layer network as well, with activation in each dense layer and dropout afterwards. In the following we list the exact training- and model details:

- number of experts = 7
- batchsize = 256
- codesize = 20
- number of iterations = 20000
- activation fct = elu
- encoder depth = 1
- encoder internal size = 100
- decoder depth = 1
- decoder internal size = 100
- loss coef reconstruct data = 1
- loss coef KL divergence standard gaussian = 0.2
- loss coef clustering = 0.8
- learning rate = 0.001
- batch normalization = True
- dropout rate = 0.5
- depth cluster network = 1
- internal size cluster network = 100
- cluster loss coef kernel = 1
- cluster loss coef depict = 1
- cluster loss entropy = 1
- trainable parameters = 13694448
- best loss = 0.11028181

B.4 Learning cell type composition in peripheral blood mononuclear cells using CyTOF measurements

The Encoder and Decoder networks are three dense layers stacked with 20 units. Results are computed setting the loss coefficient for the KL loss of the VAE equal to zero, since we do not intend to generate any data, but rather give the chance to the AE to pick up the correct subpopulations. Further model and training details for all experiments on CyTOF data:

- number of experts: 25 [5], 15 [11]
- batch size: 128
- code size: 9
- Number of iterations: 30000 [5], 20000 [11]

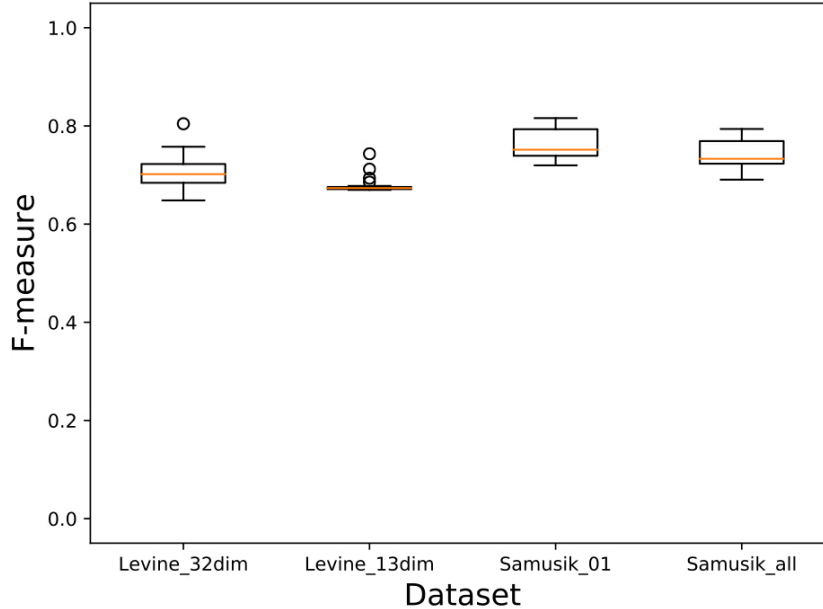


Figure B.7: The boxplots show similar as in Weter *et al.* [5] the reproducibility of MoE-Sim-VAE on the four datasets when running MoE-Sim-VAE 30 times. The variance on defining the correct subpopulations of MoE-Sim-VAE is quite small and therefore also an improvement to many methods compared in Weber *et al.*[5].

- activation function: relu
- loss coefficient data reconstruction: 1
- loss coefficient clustering : 1
- loss coefficient mixture of Gaussian: 0
- learning rate: 0.001 [5], 0.005 [11]
- batch normalization
- dropout rate: 0.5
- distance threshold (perplexity parameter): 2
- distance metric: correlation
- depth clustering network: 5
- internal size clustering network: 9
- trainable parameters: 37563 [5], 22228 [11]

Table A1: CyTOF measurements from peripheral blood mononuclear cells (PBMCs) were taken and the goal is to define the different cell types present in the data. The ground truth was defined using the SPADE algorithm [12], which can visualize the high dimensional data in such a way to be able to manual gate the cells. We compare to other fully unsupervised methods as FlowSOM, X-shift and PhenoGraph and achieve in most cases the best F-measure

Inhibitor	Well	MoE-Sim-VAE	FlowSOM	X-shift	PhenoGraph
AKTi	A02	0.7666	0.5147	0.5704	0.6588
AKTi	A03	0.7541	0.4793	0.546	0.6026
AKTi	A04	0.6815	0.6405	0.5298	0.5974
AKTi	A05	0.7127	0.7108	0.6089	0.6104
AKTi	A06	0.6711	0.7383	0.572	0.6611
AKTi	A07	0.7233	0.7034	0.5583	0.6981
AKTi	A08	0.7901	0.7024	0.4541	0.5287
AKTi	A09	0.7604	0.4292	0.5014	0.6414

AKTi	A10	0.7275	0.4952	0.4144	0.677
AKTi	A11	0.7540	0.6456	0.6673	0.6302
BTKi	A02	0.7261	0.698	0.7136	0.7478
BTKi	A03	0.7982	0.6643	0.6012	0.7141
BTKi	A04	0.7835	0.6864	0.6983	0.7103
BTKi	A05	0.7484	0.6397	0.7454	0.7474
BTKi	A06	0.8196	0.703	0.7625	0.7949
BTKi	A07	0.7976	0.6729	0.6841	0.7102
BTKi	A08	0.8108	0.6715	0.5887	0.6884
BTKi	A09	0.7789	0.5299	0.6426	0.7236
BTKi	A10	0.7726	0.6319	0.6775	0.7148
BTKi	A11	0.7857	0.6078	0.5939	0.6786
BTKi	A12	0.6600	0.5503	0.6028	0.6308
Crassin	A01	0.6727	0.6488	0.6315	0.6237
Crassin	A02	0.8225	0.557	0.6435	0.7165
Crassin	A03	0.8346	0.5736	0.6628	0.7085
Crassin	A04	0.8446	0.5348	0.7146	0.7045
Crassin	A05	0.8462	0.7444	0.6227	0.7202
Crassin	A06	0.8569	0.7448	0.7078	0.6972
Crassin	A07	0.8170	0.5164	0.6546	0.6309
Crassin	A08	0.8431	0.8283	0.5504	0.6546
Crassin	A09	0.8412	0.5814	0.6027	0.6684
Crassin	A10	0.8527	0.7537	0.6586	0.6338
Crassin	A11	0.8453	0.7174	0.6437	0.7358
Crassin	A12	0.7320	0.6161	0.6436	0.6949
Dasatinib	A01	0.7235	0.4466	0.554	0.6725
Dasatinib	A02	0.8019	0.516	0.6238	0.701
Dasatinib	A03	0.7864	0.5108	0.5366	0.6566
Dasatinib	A04	0.6661	0.4796	0.5527	0.647
Dasatinib	A05	0.7910	0.5014	0.5804	0.6904
Dasatinib	A06	0.7979	0.5167	0.6258	0.6707
Dasatinib	A07	0.8105	0.5215	0.6016	0.6809
Dasatinib	A08	0.8047	0.6928	0.5802	0.633
Dasatinib	A09	0.7485	0.5203	0.5958	0.6861
Dasatinib	A10	0.8062	0.5158	0.5742	0.6503
Dasatinib	A11	0.7837	0.5066	0.6331	0.6813
GDC-0941	A01	0.5632	0.6434	0.5987	0.6279
GDC-0941	A02	0.8257	0.7291	0.7349	0.7507
GDC-0941	A03	0.8268	0.7321	0.6822	0.7853
GDC-0941	A04	0.8389	0.7115	0.7569	0.7421
GDC-0941	A05	0.8382	0.7946	0.7171	0.7735
GDC-0941	A06	0.8463	0.6125	0.6858	0.764
GDC-0941	A07	0.8382	0.6061	0.7776	0.7612
GDC-0941	A08	0.8249	0.5493	0.6058	0.7796
GDC-0941	A09	0.8606	0.7689	0.8043	0.7206
GDC-0941	A10	0.8412	0.7227	0.653	0.6465
GDC-0941	A11	0.7859	0.5703	0.7297	0.7891
GDC-0941	A12	0.7803	0.6326	0.69	0.6727
Go69	A01	0.6520	0.6571	0.718	0.5822
Go69	A02	0.7835	0.7693	0.6075	0.7322
Go69	A03	0.7305	0.7334	0.757	0.6414
Go69	A04	0.7640	0.7456	0.8013	0.7425
Go69	A05	0.7812	0.7555	0.7294	0.7727
Go69	A06	0.7816	0.7404	0.7437	0.6443
Go69	A07	0.7407	0.8513	0.7527	0.6811
Go69	A08	0.7293	0.7338	0.6984	0.6525
Go69	A09	0.8228	0.6955	0.6985	0.7317
Go69	A10	0.7560	0.7512	0.7689	0.7071
Go69	A11	0.7565	0.7373	0.7213	0.7315

Go69	A12	0.7426	0.7086	0.7846	0.6442
H89	A01	0.6734	0.6952	0.6003	0.6105
H89	A02	0.7288	0.5391	0.5918	0.678
H89	A03	0.8051	0.5414	0.6856	0.6759
H89	A04	0.8144	0.7314	0.662	0.7287
H89	A05	0.7821	0.5468	0.6485	0.6672
H89	A06	0.7647	0.5636	0.8281	0.7165
H89	A07	0.7762	0.6983	0.7284	0.6442
H89	A09	0.8131	0.5442	0.5906	0.6707
H89	A10	0.7517	0.5549	0.6028	0.682
H89	A11	0.7417	0.7414	0.6863	0.7257
H89	A12	0.7939	0.6934	0.5831	0.6401
IKKi	A02	0.7945	0.6619	0.7371	0.6475
IKKi	A03	0.6873	0.6568	0.5661	0.6895
IKKi	A04	0.7942	0.6754	0.6386	0.7052
IKKi	A05	0.6977	0.6569	0.6157	0.6899
IKKi	A06	0.7442	0.6931	0.7024	0.7077
IKKi	A07	0.7352	0.5303	0.669	0.7001
IKKi	A08	0.7470	0.7006	0.5358	0.6869
IKKi	A09	0.8097	0.5175	0.6299	0.6969
IKKi	A10	0.7647	0.6308	0.657	0.7334
IKKi	A11	0.7878	0.6365	0.6757	0.6613
IKKi	A12	0.6673	0.5629	0.497	0.6043
Imatinib	A02	0.7935	0.7571	0.6721	0.7677
Imatinib	A03	0.7763	0.7429	0.7041	0.7499
Imatinib	A04	0.8058	0.7564	0.6921	0.7229
Imatinib	A05	0.7714	0.7559	0.6689	0.7609
Imatinib	A06	0.7756	0.746	0.6956	0.7296
Imatinib	A07	0.7468	0.7515	0.6974	0.7137
Imatinib	A08	0.7631	0.7534	0.5189	0.7096
Imatinib	A09	0.8082	0.5605	0.5819	0.7447
Imatinib	A10	0.7964	0.5645	0.5637	0.78
Imatinib	A11	0.7289	0.7664	0.7576	0.7395
Imatinib	A12	0.7012	0.8451	0.6369	0.7259
Jak1i	A02	0.8210	0.5167	0.5771	0.616
Jak1i	A03	0.7343	0.7139	0.6526	0.7133
Jak1i	A04	0.7321	0.7066	0.6346	0.7189
Jak1i	A05	0.7413	0.5163	0.6551	0.7089
Jak1i	A06	0.7244	0.5525	0.6804	0.6905
Jak1i	A07	0.7779	0.5499	0.5605	0.7099
Jak1i	A08	0.7281	0.6995	0.6021	0.6605
Jak1i	A09	0.8043	0.5064	0.6054	0.6717
Jak1i	A10	0.7801	0.5295	0.5538	0.7015
Jak1i	A11	0.7128	0.7307	0.7386	0.6812
Jak1i	A12	0.7204	0.6229	0.6321	0.6905
Jak2i	A01	0.6944	0.6379	0.6014	0.6207
Jak2i	A02	0.7961	0.664	0.6656	0.7083
Jak2i	A03	0.7629	0.6742	0.7138	0.7024
Jak2i	A04	0.7890	0.6716	0.6227	0.7072
Jak2i	A05	0.6666	0.4689	0.5314	0.6459
Jak2i	A06	0.8110	0.6474	0.6651	0.6833
Jak2i	A07	0.7595	0.6818	0.7593	0.6982
Jak2i	A08	0.8050	0.6601	0.6152	0.686
Jak2i	A09	0.8028	0.5253	0.6414	0.6501
Jak2i	A10	0.8030	0.6762	0.6067	0.6364
Jak2i	A11	0.8228	0.5398	0.694	0.7473
Jak2i	A12	0.6831	0.6214	0.5825	0.5687
Jak3i	A02	0.7986	0.7108	0.5666	0.6912
Jak3i	A03	0.7170	0.7116	0.6991	0.7001

Jak3i	A04	0.7983	0.5243	0.6654	0.691
Jak3i	A05	0.7087	0.6498	0.6884	0.7073
Jak3i	A06	0.7272	0.7244	0.654	0.7059
Jak3i	A07	0.7768	0.5167	0.696	0.735
Jak3i	A08	0.7196	0.6797	0.5946	0.7287
Jak3i	A09	0.7988	0.6918	0.6013	0.6826
Jak3i	A10	0.8026	0.7103	0.7104	0.7219
Jak3i	A11	0.7281	0.5107	0.6854	0.6614
Jak3i	A12	0.7511	0.6135	0.4861	0.61
Lcki	A01	0.7359	0.7582	0.6106	0.7201
Lcki	A02	0.7605	0.7453	0.6391	0.7696
Lcki	A03	0.8032	0.5608	0.6814	0.721
Lcki	A04	0.7608	0.5764	0.6788	0.7904
Lcki	A05	0.8210	0.5435	0.7204	0.7442
Lcki	A06	0.7564	0.7662	0.728	0.7556
Lcki	A07	0.8304	0.579	0.6992	0.696
Lcki	A08	0.7854	0.7457	0.5904	0.6972
Lcki	A09	0.8452	0.5859	0.6018	0.7569
Lcki	A10	0.7387	0.744	0.6598	0.6627
Lcki	A11	0.7835	0.7639	0.6836	0.7558
Lcki	A12	0.7467	0.8271	0.6888	0.6878
PP2	A02	0.7687	0.759	0.7717	0.7605
PP2	A03	0.8395	0.7644	0.7304	0.7953
PP2	A04	0.8442	0.7703	0.7116	0.7162
PP2	A05	0.8248	0.5777	0.7205	0.7547
PP2	A06	0.7866	0.7612	0.7461	0.7431
PP2	A07	0.8595	0.7616	0.724	0.7213
PP2	A08	0.8505	0.7489	0.7109	0.7195
PP2	A09	0.7902	0.5755	0.6511	0.7738
PP2	A10	0.8089	0.743	0.6635	0.7389
PP2	A11	0.7977	0.5852	0.6564	0.7846
PP2	A12	0.7667	0.6012	0.6524	0.6636
Rapamycin	A01	0.7028	0.675	0.5882	0.5677
Rapamycin	A02	0.7215	0.6831	0.6124	0.6697
Rapamycin	A03	0.7322	0.6707	0.6296	0.6861
Rapamycin	A04	0.6787	0.6696	0.6887	0.7267
Rapamycin	A05	0.7231	0.653	0.7134	0.6466
Rapamycin	A06	0.7310	0.6473	0.7009	0.6386
Rapamycin	A07	0.7595	0.6642	0.748	0.5882
Rapamycin	A08	0.7773	0.836	0.6371	0.571
Rapamycin	A09	0.7732	0.6573	0.6826	0.6615
Rapamycin	A10	0.7586	0.6702	0.7136	0.6344
Rapamycin	A12	0.6955	0.6361	0.6561	0.5472
SB202	A01	0.6884	0.6713	0.941	0.7101
SB202	A03	0.7869	0.7549	0.6686	0.7633
SB202	A05	0.7856	0.5564	0.7387	0.6999
SB202	A06	0.7707	0.755	0.7913	0.7869
SB202	A10	0.7559	0.7554	-	0.7749
SP6	A01	0.7033	0.6882	0.4191	0.532
SP6	A02	0.7536	0.5035	0.5104	0.657
SP6	A03	0.7387	0.6973	0.534	0.5858
SP6	A04	0.6910	0.503	0.5065	0.5975
SP6	A05	0.7210	0.5068	0.5643	0.6869
SP6	A06	0.7052	0.719	0.5063	0.6384
SP6	A07	0.7281	0.7074	0.5382	0.6501
SP6	A08	0.7301	0.6832	0.4665	0.6133
SP6	A09	0.7743	0.5001	0.4618	0.6208
SP6	A10	0.7198	0.5111	0.524	0.6773
SP6	A11	0.7494	0.493	0.5407	0.5935

SP6	A12	0.7311	0.6131	0.4488	0.6198
Sorafenib	A01	0.7185	0.7217	0.5884	0.6574
Sorafenib	A02	0.8250	0.7659	0.6658	0.7664
Sorafenib	A03	0.7689	0.7732	0.7078	0.6869
Sorafenib	A04	0.8360	0.7094	0.7114	0.7218
Sorafenib	A05	0.8304	0.5571	0.7672	0.7153
Sorafenib	A06	0.8021	0.5783	0.6991	0.7506
Sorafenib	A07	0.8461	0.7051	0.7267	0.6701
Sorafenib	A09	0.8226	0.7275	0.7522	0.7587
Sorafenib	A10	0.8103	0.7561	0.7457	0.7214
Sorafenib	A11	0.8465	0.5777	0.7192	0.7503
Sorafenib	A12	0.7715	0.6533	0.6084	0.6129
Staurosporine	A01	0.7985	0.8464	0.6057	0.5945
Staurosporine	A02	0.8347	0.8312	0.5999	0.6626
Staurosporine	A03	0.8079	0.7072	0.6704	0.6787
Staurosporine	A04	0.8418	0.8666	0.6452	0.6776
Staurosporine	A05	0.8657	0.7305	0.7071	0.7515
Staurosporine	A06	0.8694	0.516	0.6453	0.6619
Staurosporine	A07	0.8277	0.7052	0.6349	0.6657
Staurosporine	A08	0.8310	0.8316	0.6213	0.678
Staurosporine	A09	0.8319	0.5117	0.6747	0.6726
Staurosporine	A10	0.8417	0.5108	0.6211	0.7126
Staurosporine	A11	0.8246	0.8711	0.6547	0.7445
Streptonigrin	A01	0.7128	0.5689	0.6571	0.6599
Streptonigrin	A02	0.7836	0.5095	0.549	0.6155
Streptonigrin	A03	0.7776	0.547	0.6497	0.6527
Streptonigrin	A04	0.8466	0.7521	0.5762	0.7061
Streptonigrin	A05	0.8130	0.5406	0.6459	0.6928
Streptonigrin	A06	0.8031	0.7409	0.6446	0.6343
Streptonigrin	A07	0.7987	0.5353	0.5882	0.6657
Streptonigrin	A08	0.7470	0.7458	0.5864	0.6443
Streptonigrin	A09	0.7586	0.7034	0.5928	0.6196
Streptonigrin	A10	0.7159	0.6974	0.5174	0.6809
Streptonigrin	A11	0.8178	0.5649	0.593	0.6814
Streptonigrin	A12	0.7410	0.6034	0.5896	0.6286
Sunitinib	A01	0.7152	0.6622	0.5653	0.6522
Sunitinib	A02	0.8056	0.498	0.6138	0.6521
Sunitinib	A03	0.8095	0.6873	0.6889	0.6913
Sunitinib	A04	0.8142	0.6925	0.6467	0.7121
Sunitinib	A05	0.8157	0.6959	0.673	0.7073
Sunitinib	A06	0.7968	0.5061	0.6654	0.7025
Sunitinib	A07	0.8110	0.7	0.6333	0.6572
Sunitinib	A08	0.8186	0.6894	0.5999	0.674
Sunitinib	A09	0.8029	0.4886	0.6699	0.6621
Sunitinib	A10	0.8126	0.848	0.6087	0.6713
Sunitinib	A11	0.8241	0.824	0.6408	0.6811
Sunitinib	A12	0.7747	0.7898	0.5942	0.5867
Syki	A02	0.7682	0.7073	0.6636	0.685
Syki	A03	0.7224	0.7042	0.6424	0.7116
Syki	A04	0.7461	0.7069	0.7908	0.7256
Syki	A05	0.7468	0.7182	0.6263	0.6804
Syki	A06	0.7381	0.7134	0.7718	0.7154
Syki	A07	0.7891	0.7	0.7434	0.6479
Syki	A08	0.7509	0.7154	0.6903	0.6542
Syki	A09	0.7712	0.73	0.7357	0.6918
Syki	A10	0.7695	0.7531	0.7197	0.7242
Syki	A11	0.7360	0.7311	0.7577	0.78
Syki	A12	0.6717	0.6793	0.7426	0.7123
U0126	A01	0.6844	0.6178	-	0.6486

U0126	A02	0.8440	0.5545	0.5362	0.7043
U0126	A03	0.8340	0.5346	0.616	0.6881
U0126	A04	0.8263	0.7079	0.6166	0.7059
U0126	A05	0.8535	0.5468	0.7091	0.7031
U0126	A06	0.8199	0.5285	0.6018	0.6874
U0126	A07	0.8079	0.5304	0.5671	0.7249
U0126	A08	0.8278	0.6864	0.5359	0.6577
U0126	A09	0.8331	0.5394	0.5678	0.6967
U0126	A10	0.8436	0.5593	0.6092	0.6867
U0126	A11	0.7654	0.5072	0.6374	0.6767
U0126	A12	0.7227	0.6496	0.6253	0.6281
VX680	A01	0.6930	0.4818	0.6028	0.6452
VX680	A02	0.7340	0.711	0.5587	0.633
VX680	A03	0.7525	0.6976	0.5663	0.7292
VX680	A04	0.8127	0.6435	0.6722	0.5954
VX680	A05	0.6937	0.6742	0.7374	0.6454
VX680	A06	0.7168	0.7101	0.5769	0.6202
VX680	A07	0.7663	0.4944	0.5382	0.718
VX680	A08	0.7315	0.7082	0.4753	0.6482
VX680	A09	0.7703	0.7054	0.5859	0.6722
VX680	A10	0.7143	0.7137	0.6648	0.6167
VX680	A11	0.7050	0.6773	0.7269	0.6947
VX680	A12	0.7852	0.7922	0.5583	0.6808

References

- [1] Elie Aljalbout, Vladimir Golkov, Yawar Siddiqui, Maximilian Strobel, Daniel Cremers Clustering with Deep Learning: Taxonomy and New Methods. arXiv, 2018.
- [2] Zhuxi Jiang, Yin Zheng, Huachun Tan, Bangsheng Tang, Hanning Zhou Variational Deep Embedding: An Unsupervised and Generative Approach to Clustering. arXiv, 2017.
- [3] Leland McInnes, John Healy, James Melville UMAP: Uniform Manifold Approximation and Projection for Dimension Reduction. arXiv, 2018.
- [4] N. Aghaeepour, G. Finak, FlowCAP Consortium, DREAM Consortium, H. Hoos, TR. Mosmann, R. Brinkman, R. Gottardo, Rh. Scheuermann Critical assessment of automated flow cytometry data analysis techniques. Nature Methods, 2013.
- [5] Lukas M. Weber, Mark D. Robinson Comparison of clustering methods for high-dimensional single-cell flow and mass cytometry data. Cytometry Part A, 2016.
- [6] Noam Shazeer, Azalia Mirhoseini, Krzysztof Maziarz, Andy Davis, Quoc Le1, Geoffrey Hinton, Jeff Dean Outrageously Large Neural Networks: The Sparsely-Gated Mixture-of-Experts Layers. arXiv, 2017.
- [7] Kamran Ghasedi Dizaji, Amirhossein Herandi, Cheng Deng, Weidong Cai, Heng Huang Deep Clustering via Joint Convolutional Autoencoder Embedding and Relative Entropy Minimization. arXiv, 2017.
- [8] Sofie Van Gassen, Britt Callebaut, Mary J. Van Helden, Bart N. Lambrecht, Piet Demeester, Tom Dhaene, Yvan Saeys FlowSOM: Using self-organizing maps for visualization and interpretation of cytometry data. Cytometry Part A, 2015.
- [9] Nikolay Samusik, Zinaida Good, Matthew H. Spitzer, Kara L. Davis, Garry P. Nolan Automated Mapping of Phenotype Space with Single-Cell Data. Nature Methods, 2016.
- [10] Jacob H. Levine, Erin F. Simonds, Sean C. Bendall, Kara L. Davis, El-ad D. Amir, Michelle D. Tadmor, Oren Litvin, Harris G. Fienberg, Astraea Jager, Eli R. Zunder, Rachel Finck, Amanda L. Gedman, Ina Radtke, James R. Downing, Dana Pe’er, Garry P. Nolan Data-Driven Phenotypic Dissection of AML Reveals Progenitor-like Cells that Correlate with Prognosis. Cell, 2015.
- [11] Bernd Bodenmiller, Eli R. Zunder, Rachel Finck, Tiffany J. Chen, Erica S. Savig, Robert V. Bruggner, Erin F. Simonds, Sean C. Bendall, Karen Sachs, Peter O. Krutzik, Garry P. Nolan Multiplexed mass cytometry profiling of cellular states perturbed by small-molecule regulators. Nature Biotechnology, 2012.

- [12] Peng Qiu, Erin F. Simonds, Sean C. Bendall, Kenneth D. Gibbs Jr., Robert V. Bruggner, Michael D. Linderman, Karen Sachs, Garry P. Nolan, Sylvia K. Plevritis Extracting a cellular hierarchy from high-dimensional cytometry data with SPADE. *Nature Biotechnology*, 2011.
- [13] Eirini Arvaniti, Manfred Claassen Sensitive detection of rare disease-associated cell subsets via representation learning. *Nature Communications*, 2017.
- [14] Arthur Gretton, Karsten Borgwardt, Malte J. Rasch, Bernhard Scholkopf, Alexander J. Smola A Kernel Method for the Two-Sample Problem. *arXiv*, 2008.
- [15] Dougal J. Sutherland, Hsiao-Yu Tung, Heiko Strathmann, Soumyajit De, Aaditya Ramdas, Alex Smola, Arthur Gretton Generative models and model criticism via optimized maximum mean discrepancy. *arXiv*, 2019.
- [16] D. P. Kingma, M. Welling Auto-Encoding Variational Bayes. *International Conference on Learning Representations (ICLR)*, 2014.
- [17] Christopher M. Bishop *Pattern Recognition and Machine Learning*. Springer, 2006.
- [18] Alexander W. Kay, Dara M. Strauss-Albee, Catherine A. Blish Application of Mass Cytometry (CyTOF) for Functional and Phenotypic Analysis of Natural Killer Cells. *Methods in Molecular Biology*, 2013.
- [19] Bo Yang, Xiao Fu, Nicholas D. Sidiropoulos, Mingyi Hong Towards K-means-friendly Spaces: Simultaneous Deep Learning and Clustering. *arXiv*, 2017.
- [20] Erxue Min, Xifeng Guo, Qiang Liu, Gen Zhang, Jianjing Cui, Jun Long A Survey of Clustering With Deep Learning: From the Perspective of Network Architecture. *IEEE*, 2018.
- [21] Dejjiao Zhang, Yifan Sun, Brian Eriksson, Laura Balzano Deep Unsupervised Clustering Using Mixture of Autoencoders. *arXiv*, 2017.
- [22] S. Chopra, R. Hadsell, Y. LeCun Learning a similarity metric discriminatively, with application to face verification. *IEEE*, 2005.
- [23] Jasmine Irani, Nitin Pise, Madhura Phatak Clustering Techniques and the Similarity Measures used in Clustering: A Survey. *International Journal of Computer Applications*, 2016.
- [24] Laurens van der Maaten, Geoffrey Hinton Visualizing Data using t-SNE. *Journal of Machine Learning Research*, 2008.
- [25] J. Yang, D. Parikh, D. Batra Joint unsupervised learning of deep representations and image clusters. *Proceedings of the IEEE Conference on Computer Vision and Pattern Recognition (CVPR)*, 2016b.
- [26] C.-C. Hsu, C.-W. Lin Cnn-based joint clustering and representation learning with feature drift compensation for large-scale image data. *arXiv*, 2017.
- [27] J. Xie, R. Girshick, A. Farhadi Unsupervised deep embedding for clustering analysis. *International Conference on Machine Learning (ICML)*, 2016.
- [28] F. Li, H. Qiao, B. Zhang, X. Xi Discriminatively boosted image clustering with fully convolutional autoencoders. *arXiv*, 2017.
- [29] S. Saito, R. T. Tan Neural clustering: Concatenating layers for better projections. *Workshop track at ICLR*, 2017.
- [30] D. Chen, J. Lv, Z. Yi Unsupervised multi-manifold clustering by learning deep representation. *Workshops at the AAAI Conference on Artificial Intelligence*, 2017.
- [31] Z. Wang, S. Chang, J. Zhou, M. Wang, T. S. Huang Learning a task-specific deep architecture for clustering. *Proceedings of the SIAM International Conference on Data Mining (ICDM)*, 2016.
- [32] W. Hu, T. Miyato, S. Tokui, E. Matsumoto, M. Sugiyama Learning discrete representations via information maximizing self augmented training. *arXiv*, 2017.
- [33] Vincent Fortuin, Matthias Hüser, Francesco Locatello, Heiko Strathmann, Gunnar Rätsch SOM-VAE: Interpretable Discrete Representation Learning on Time Series. *Conference paper at ICLR*, 2019.
- [34] Uri Shaham, Kelly Stanton, Henry Li, Boaz Nadler, Ronen Basri, Yuval Kluger SpectralNet: Spectral Clustering using Deep Neural Networks. *Published as a conference paper at ICLR*, 2018.
- [35] Christopher M. Bishop *Neural Networks for Pattern Recognition*, CLARENDON PRESS, 1995.
- [36] The Tabula Muris Consortium., Overall coordination., Schaum, N. *et al.* Single-cell transcriptomics of 20 mouse organs creates a Tabula Muris *Nature* 562, 367–372 (2018). <https://doi.org/10.1038/s41586-018-0590-4>.
- [37] Li, B., Qing, T., Zhu, J. *et al.* A Comprehensive Mouse Transcriptomic BodyMap across 17 Tissues by RNA-seq *Sci Rep* 7, 4200 (2017). <https://doi.org/10.1038/s41598-017-04520-z>.

- [38] Chad M. Trent, Shuiqing Yu, Yunying Hu, Nathan Skoller, Lesley A. Huggins, Shunichi Homma, Ira J. Goldberg Lipoprotein lipase activity is required for cardiac lipid droplet production *J Lipid Res.* (2014)
- [39] Hiroaki Yagyu, Guangping Chen, Masayoshi Yokoyama, Kumiko Hirata, Ayanna Augustus, Yuko Kako, Toru Seo, Yunying Hu, E. Peer Lutz, Martin Merkel, André Bensadoun, Shunichi Homma, Ira J. Goldberg Lipoprotein lipase (LpL) on the surface of cardiomyocytes increases lipid uptake and produces a cardiomyopathy *J Clin Invest.* (2003)
- [40] Chao Feng, Shufen Liu, Hao Zhang, Renchu Guan, Dan Li, Fengfeng Zhou, Yanchun Liang, Xiaoyue Feng Dimension Reduction and Clustering Models for Single-Cell RNA Sequencing Data: A Comparative Study *Int J Mol Sci.* (2020)
- [41] L. McInnes, J. Healy, S. Astels hdbSCAN: Hierarchical density based clustering In: *Journal of Open Source Software The Open Journal*, volume 2, number 11. (2017)
- [42] Madson Luiz Dantas Dias fuzzy-c-means: An implementation of Fuzzy *C*-means clustering algorithm *Zenodo* (2019), 10.5281/zenodo.3066222
- [43] Feng Yue *et al.* A comparative encyclopedia of DNA elements in the mouse genome *Nature.* (2014)
- [44] Lance Godfrey N. and Williams William T. Computer programs for hierarchical polythetic classification ("similarity analysis") *Computer Journal* (1966), doi:10.1093/comjnl/9.1.60